PERGAMON

International Journal of Heat and Mass Transfer 45 (2002) 4463–4477

International Journal of HEAT and MASS TRANSFER

www.elsevier.com/locate/ijhmt

Experimental and theoretical study of orientation effects on flow boiling CHF

Hui Zhang [a], Issam Mudawar [a,*], Mohammad M. Hasan [b]

[a] *Boiling and Two-phase Flow Laboratory, School of Mechanical Engineering, Purdue University, 1288 Mechanical Engineering Building, West Lafayette, IN 47907, USA*

[b] *NASA Glenn Research Center, 21000 Brookpark Road, Cleveland, OH 44135, USA*

Received 28 February 2002; received in revised form 11 April 2002

Abstract

The effects of orientation on flow boiling critical heat flux (CHF) were investigated using high-speed video and microphotographic techniques. Interfacial features were measured just prior to CHF and statistically analyzed. A dominant wavy vapor layer regime was observed for all relatively high-velocities and most orientations, while several other regimes were encountered at low velocities, in downflow and/or downward-facing heated wall orientations. The interfacial lift-off model was modified and used to predict the orientation effects on CHF for the dominant wavy vapor layer regime. The photographic study revealed a fairly continuous wavy vapor layer travelling along the heated wall while permitting liquid contact only in wetting fronts, located in the troughs of the interfacial waves. The waves, which were generated at an upstream location, had a tendency to preserve a curvature ratio as they propagated along the heated wall. CHF commenced when wetting fronts near the outlet were lifted off the wall. This occurred when the momentum of vapor normal to the wall exceeded the pressure force associated with interfacial curvature. The interfacial lift-off model is shown to be very effective at capturing the overall dependence of CHF on orientation.

Keywords: Critical heat flux; Flow boiling; Orientation

1. Introduction

1.1. Flow boiling CHF mechanisms and models

The critical heat flux (CHF) mechanism have been the focus of numerous studies dating back to the 1940s. Much of the earlier research was concerned with steam generation in nuclear reactor vessels and conventional power plant boilers. CHF prediction today remains largely empirical in the absence of a widely accepted mechanism or model that can tackle different fluids, flow geometries and operating conditions. Strong disagreements still exist among investigators over the near-wall conditions just before CHF, the CHF *trigger* mechanism, and the combined influence of global parameters (pressure, mass velocity, inlet subcooling, hydraulic diameter, and heated length) on CHF.

Four main types of models encompass virtually all research concerning flow boiling CHF inside channels: *boundary layer separation*, *bubble crowding*, *sublayer dryout*, and *interfacial lift-off*. The boundary layer separation models are based on predicting the rate of vapor production normal to the wall that causes the bulk liquid flow to separate from the wall due to a substantial diminution in the near-wall liquid velocity gradient [1,2]. The bubble crowding models postulate that CHF occurs when turbulent fluctuations in the liquid flow become too weak to transport liquid through the bubbly layer [3,4]. The sublayer dryout models assume CHF occurs once the heat supplied at the wall exceeds the enthalpy of liquid replenishing a thin sublayer which forms beneath

* Corresponding author. Tel.: +1-765-494-5705; fax: +1-765-494-0539.

E-mail address: mudawar@ecn.purdue.edu (I. Mudawar).

0017-9310/02/$ - see front matter
PII: S0017-9310(02)00152-7

Nomenclature

A	channel cross-sectional area
A_k	cross-sectional area occupied by phase k
A_w	area of wetting front
b	ratio of wetting front length to wavelength, w/λ
c	wave speed
$C_{f,i}$	interfacial friction factor
c_i	imaginary component of wave speed
$c_{p,f}$	specific heat of liquid
D_f	hydraulic diameter of liquid layer, $2W(H-\delta)/(W+H-\delta)$
D_g	hydraulic diameter of vapor layer, $2W\delta/(W+\delta)$
f_k	wall friction factor for phase k
g	earth's gravitational acceleration
g_n	component of gravitational acceleration normal to wall, $g\cos\theta$
G	mass flux, $\rho_f U$
H	channel height (5 mm)
h_{fg}	latent heat of vaporization
H_k	height (thickness) of phase k layer
h_{meas}	measured vapor patch height
k	wave number, $2\pi/\lambda$
k_c	critical wave number, $2\pi/\lambda_c$
L	heater length in flow direction (101.6 mm)
P	pressure
p_i	interfacial perimeter between phases
p_k	perimeter of wall contact with phase k
P_o	outlet pressure
q''	wall heat flux
q''_m	critical heat flux
q''_w	wetting front lift-off heat flux
t	time
T	temperature
$\Delta T_{sub,i}$	inlet subcooling, $T_{sat,i}-T_{b,i}$
$\Delta T_{sub,o}$	calculated outlet subcooling, $T_{sat,o}-T_{b,o}$
U	mean liquid inlet velocity
U_f	liquid phase velocity
U_g	vapor phase velocity
$U_{g,n}$	vapor velocity in wetting front normal to wall
u_i	streamwise velocity of vapor produced at interface
w	wetting front length used in CHF model
W	heater and channel width (2.5 mm)
W'_{fg}	rate of interfacial evaporation per unit streamwise distance
w_j	length of jth wetting front
w_{meas}	measured wetting front length
x	flow quality
z	streamwise coordinate
z^*	extent of continuous upstream wetting region
z_0	streamwise distance where $U_f = U_g$

Greek symbols

α	void fraction, δ/H
δ	mean vapor layer thickness; vapor layer amplitude used in CHF model
η	interfacial perturbation
η_0	amplitude of interfacial perturbation, $\eta_0=\delta$
θ	flow orientation angle
λ	vapor wavelength
λ_c	critical wavelength
λ_j	wavelength of jth wave
λ_{meas}	measured vapor patch length
ρ_f	density of saturated liquid
ρ''_f	modified liquid density
ρ_g	density of saturated vapor
ρ''_g	modified vapor density
σ	surface tension
τ_i	interfacial shear stress
$\tau_{w,f}$	shear stress between wall and liquid
$\tau_{w,g}$	shear stress between wall and vapor

Subscripts

b	bulk liquid
f	saturated liquid
g	saturated vapor
i	inlet; imaginary component
k	phase k ($k=f$ for liquid or g for vapor)
m	maximum, critical heat flux
o	outlet
sat	saturation
w	wall

oblong, coalescent vapor bubbles [5]. The latter model was based on the assumption that the length of coalescent bubbles can only grow to the Helmholtz wavelength since bubbles which are longer than the Helmholtz wavelength should become unstable and break up into shorter bubbles.

One of the earliest and most systematic depictions of the near-wall interfacial behavior was undertaken by Hino and Ueda [6,7], who employed microthermocouples to determine bubble frequency and the vapor residence period near the wall. Long periods of high-temperature fluctuation revealed discrete bubbles are replaced by a fairly continuous wavy vapor layer at heat fluxes even below CHF. The interfacial lift-off model, proposed by Galloway and Mudawar [8,9] in the early 1990s, is based upon this wavy vapor layer depiction.

This model postulates that (1) the wavy layer makes contact with the wall only at discrete wetting fronts corresponding to the vapor layer troughs, and (2) CHF is initiated by lift-off of the wetting fronts from the wall due to intense vapor momentum. Unlike previous CHF models, the interfacial lift-off model was experimentally validated by Galloway and Mudawar using photographic tracking of the vapor–liquid interface using high-speed video and photomicrographic methods [8,9]. Sturgis and Mudawar [10,11] improved the original interfacial lift-off model by deriving an analytical expression for the lift-off heat flux and broadening the applicability range of the model; the improved model was intended for horizontal flows.

While most attention in CHF modeling has been focussed on vertical upflow prevalent in nuclear reactors and steam boilers, new applications began to emerge which demanded intense heat dissipation from relatively small surfaces (e.g., cooling of microprocessors, lasers, X-ray anodes), in low gravity (e.g., space shuttle, International space station, satellites), as well as in fluctuating "g" fields (e.g., fighter aircraft). Those and other applications have shifted the focus in CHF modeling to more complex operating environments. The present study was motivated by a need to better understand the effects of reduced gravity on flow boiling CHF in space systems. In a terrestrial testing environment, changing flow orientation is one means of producing "partial" gravity in the direction of fluid flow or perpendicular to a heated wall.

1.2. Effects of orientation on flow boiling CHF

Howard and Mudawar [12] investigated the effects of wall orientation on pool boiling CHF. They showed orientation effects fall into three regions; each is associated with a unique CHF trigger mechanism. In the upward-facing region, the buoyancy forces remove the vapor vertically off the wall in accordance with the classical interpretation by Zuber et al. [13]. In the downward-facing region, the vapor stratifies beneath the heated wall, resulting in very small CHF values. The near-vertical region is characterized by a wavy liquid–vapor interface very similar to that proposed earlier for flow boiling by Galloway and Mudawar [8,9] and Sturgis and Mudawar [10,11]. Howard and Mudawar adapted the interfacial lift-off model to accurately predict near-vertical region CHF data.

Orientation effects in flow boiling are complicated by the influence of liquid inertia. Buoyancy plays a dominant role at low velocities due to weak inertia, which results in lower CHF values for downflow, for example, compared to upflow at the same velocity. Increasing the liquid velocity imparts greater significance to liquid inertia. In fact, high velocities can completely negate the effects of orientation, producing virtually equal CHF for downflow as for upflow. These trends were confirmed by Simoneau and Simon [14] and Mishima and Nishihara [15]. Both studies showed vapor motion in a vertical downflow switches from concurrent at high-liquid velocities to countercurrent at low velocities. Mishima and Nishihara suggested flooding is the cause of CHF for downflow at very low velocities. They also identified a very low CHF downflow condition where bubbles stagnate upon the heated wall because of a balance between liquid inertia and buoyancy force.

In a previous paper by the authors of the present study [16], the effects of orientation on flow boiling CHF were investigated experimentally at eight orientations spaced 45° apart using FC-72 as working fluid. Fig. 1 provides a definition of flow orientation as well as the location of the heated wall for each orientation. Orientation angle is referenced to the $\theta = 0°$ horizontal orientation with the heated wall facing upwards. Based on photographic results, six CHF regimes were identified for saturated flow, which are represented in Fig. 2:

1. wavy vapor layer,
2. pool boiling,
3. stratification of vapor above liquid,
4. vapor stagnation,
5. vapor counterflow, and
6. separated concurrent vapor flow.

The low velocity, upward-facing heated wall data were underpredicted by the Zuber et al. model [13] for pool boiling. The vapor stagnation, vapor counterflow, and vapor concurrent flow data seemed closely related to flooding. The wavy vapor layer regime encompassed

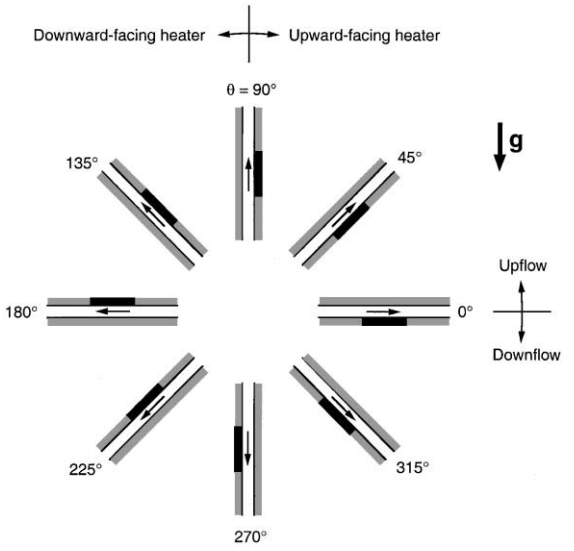

Fig. 1. Flow orientation nomenclature. Heater location for each orientation is identified by a black rectangle.

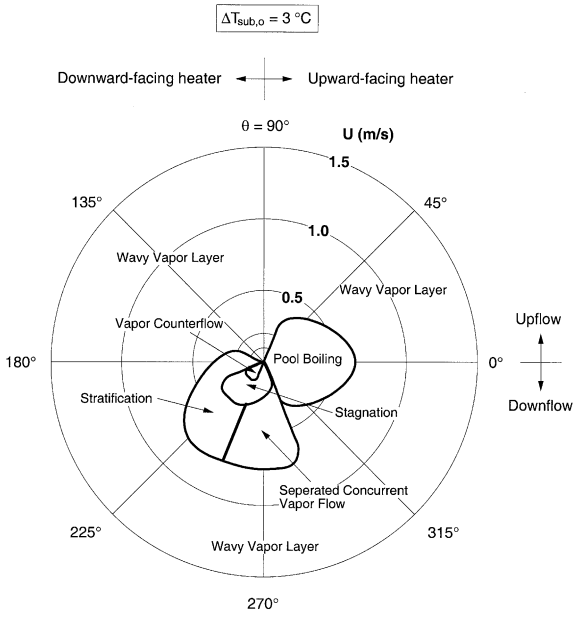

Fig. 2. CHF regimes for saturated flow [16].

high-velocity conditions at all orientations, as well as low-velocity upflow orientations. CHF data belonging to the wavy vapor layer regime were within the range of Sturgis and Mudawar's [10,11] interfacial lift-off model predictions. Since this model was developed for horizontal flow, the predictions did not distinguish between different flow orientations, and resulted in equal CHF for all orientations corresponding to the same velocity.

In this paper, the interfacial lift-off model is modified to explore the effects of gravitational force on near-saturated flow boiling CHF for operating conditions falling into the wavy layer regime. Extensive high-speed video images are statistically analyzed to characterize the wavy layer interfacial features for different orientations. The modified model predictions are verified with measured CHF data.

2. Experimental methods

CHF tests were performed using a two-phase flow loop which conditioned FC-72 to the desired pressure, temperature and flow rate at the inlet to the flow boiling module. The module consisted of two transparent polycarbonate plastic (Lexan) plates which sandwiched a heater block made from high-purity oxygen-free copper. As shown in Fig. 3, a 5.0×2.5 mm (shorter dimension corresponds to the heater width) flow channel was milled into the bottom plate of the flow module. The conditioned liquid entered the channel through an enlarged rectangular cavity containing a honeycomb flow straightener. The upstream edge of the heater wall was

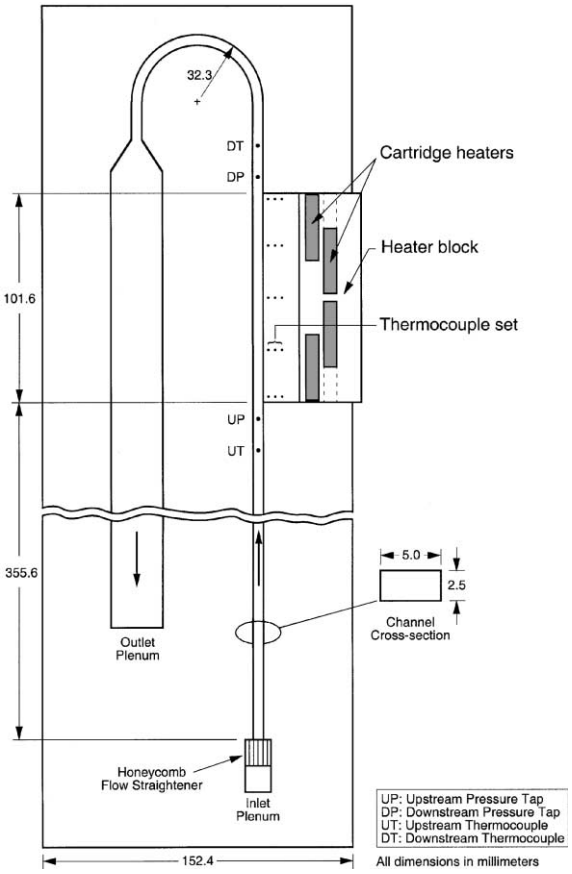

Fig. 3. Bottom plate of flow boiling module.

situated 355.6 mm from the inlet, allowing the flow to become fully developed before entering the heated region. The fluid was heated over a 101.6 mm length before returning as a two-phase mixture to the conditioning loop via an enlarged exit channel in the bottom plate.

The heated wall is the edge of a thin section which protruded from a bulkier section of the same copper block, where high-power density cartridge heaters were embedded. Wall temperature and wall heat flux were both determined from readings of five thermocouple arrays (each containing three thermocouples) strategically located along the heated length. The heat flux and wall temperature were determined with 7.9% and 0.3 °C uncertainty, respectively. Further details concerning experimental uncertainty, flow loop construction, and experimental methods are available in [16].

Fig. 1 illustrated the definition of flow orientation adopted in the present study. The orientation angle increases counterclockwise, with horizontal flow and an upward-facing wall defining the $\theta = 0°$ datum. Eight different orientations corresponding to increments of 45° were chosen to represent all possible orientation effects.

For each orientation, CHF was measured using FC-72 for five flow velocities ($U = 0.1$, 0.2, 0.5, 1 and 1.5 m/s), a constant outlet pressure of $P_o = 138$ kPa (20 psia), and near-saturated outlet subcooling of $\Delta T_{sub,o} = 3$ °C.

3. Statistical characterization of interfacial features

3.1. Wavy vapor layer development

As indicated in Fig. 2, six CHF regimes have been previously identified by the authors for saturated flow. The present paper concerns modeling of CHF corresponding to the wavy vapor layer regime, which was observed for most velocities and orientations.

In the present study, a 2 s video sequence was recorded at a rate of 1000 frames/s at the middle and outlet sections of the heated wall. Figs. 4–6 depict the development of the wavy vapor layer just prior to CHF at $\theta = 135°$ for $U = 0.5$, 1 and 1.5 m/s, respectively. This orientation is chosen because the wavy vapor layer was observed for all three velocities. Seventeen sequential video frames are presented in each figure for each of the middle and outlet sections. The bottom edge of each image represents the heated wall and the upper edge the opposite plastic wall of the flow channel. The time elapsed between consecutive frames is 0.00025 s. Aside from enabling the sizing of interfacial features, the sequential frames facilitate tracking the propagation of the wavy vapor layer along the heated wall. Figs. 4–6 clearly support Galloway and Mudawar's [8,9] depiction of a fairly continuous wavy vapor layer (which develops prior to CHF) travelling along the wall while permitting liquid contact only in wetting fronts, located in the troughs of the interfacial waves.

Interfacial parameters describing both the size and shape of the wavy vapor layer were carefully measured and statistically averaged to explore the vapor layer's development along the heated wall. These parameters, which are illustrated in Fig. 7a, consist of vapor "patch" length, λ_{meas}, maximum height, h_{meas}, and length of region of liquid contact with the surface between adjacent patches, w_{meas}. The measured dimensions were averaged for sets of 30 frames, which was deemed a statistically acceptable sample since additional frames had little effect on the calculated average.

The CHF interfacial lift-off model is based on an idealized sinusoidal liquid–vapor interface characterized by a wavelength, λ, and amplitude, δ, as illustrated in Fig. 7b. The idealized wavelength is defined as the distance between consecutive wetting fronts, hence it is the sum of average vapor length and average wetting front length. When approximating a series of observed vapor patches with a sinusoidal profile, the interfacial amplitude is half the measured average height, and the wetting front length of the idealized interface is the same as the measured one. Therefore, the following definitions relate the measured quantities to the idealized ones,

$$\lambda = \bar{\lambda}_{meas} + \bar{w}_{meas}, \tag{1}$$

$$\delta = \frac{1}{2}\bar{h}_{meas} \tag{2}$$

and

$$w = \bar{w}_{meas}. \tag{3}$$

Poor lighting for certain velocities and orientations prevented the capture of high-resolution frames from which interfacial measurements could be made. Therefore, the data for those cases are not available. Furthermore, velocities of 0.5 m/s or smaller produced vapor patches which extended beyond the length of the video frame and could not be accurately sized. Table 1 shows the interfacial characteristics for conditions which could be carefully measured and statistically characterized. At the outlet section, the wavelength, λ, and amplitude, δ, of the vapor layer both increase compared with those in the middle section, as depicted in Figs. 4–6. The wetting front length, w, between adjacent vapor patches also increases in the flow direction. Statistical averages for each section reveal this wetting front length increases in proportion to the vapor wavelength such that it remains approximately the same fraction of the interfacial wavelength, λ. This is indicated by a ratio, b, defined as

$$b = \frac{w}{\lambda}. \tag{4}$$

As shown in Table 1, this ratio is fairly insensitive to velocity or flow orientation for the wavy vapor layer regime.

4. CHF model

4.1. Rationale

The present model is based on the observation that a wavy liquid–vapor interface develops along the heated wall and permits liquid cooling only in discrete wetting fronts. Therefore, the heat is transferred to the liquid by means of vigorous boiling only in the wetting fronts. The interfacial waviness is a result of instability between the liquid and vapor phases. The phase velocity difference acts as a destabilizing effect while surface tension tends to maintain interfacial stability. Body force may be stabilizing or destabilizing depending on the surface orientation with respect to gravity. In the wetting fronts, the momentum associated with the vapor effusion tends to push the interface away from the heated wall. This momentum is resisted by a pressure force associated with interfacial curvature. When the vapor momentum

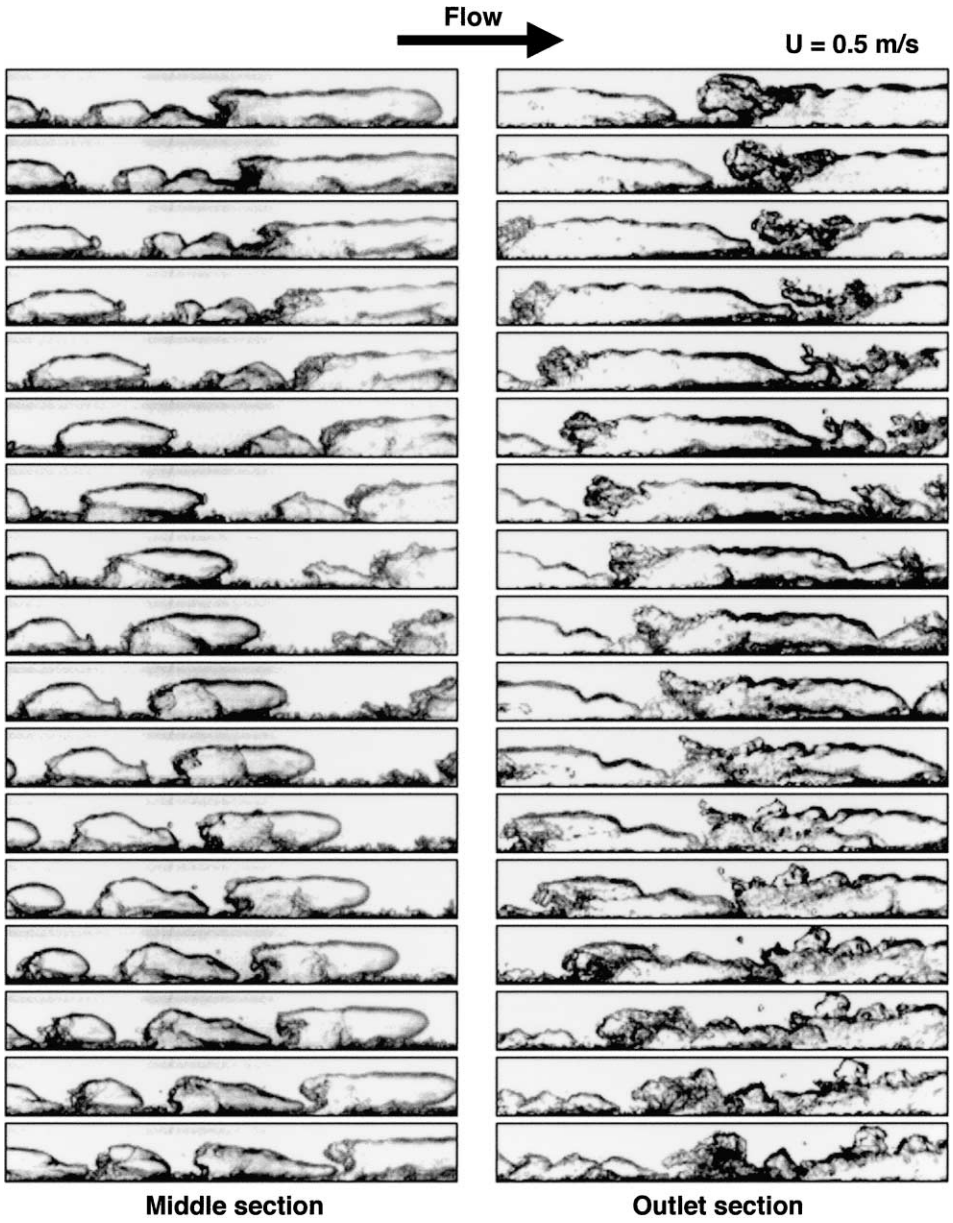

Fig. 4. Sequential images of wavy vapor layer at $\theta = 135°$, $\Delta T_{sub,o} = 3$ °C and $U = 0.5$ m/s.

at a wetting front overcomes the pressure force, the interface will be lifted from the wall and heat transfer at the wetting front is eliminated. Heat that would otherwise be dissipated at this wetting front will now have to be channeled to neighboring wetting fronts. Increased heat transfer in these neighboring wetting fronts greatly intensifies the vapor momentum perpendicular to the wall, creating conditions which are more favorable for lift-off at those wetting fronts as well. A chain reaction thus ensues, where wetting fronts are eliminated in succession, and the lift-off process actually accelerates with time as more heat has to be dissipated from a decreasing number of wetting fronts. This explains why flow boiling CHF is often described as a catastrophic rather than slow or gradual phenomenon.

In the present study, the interfacial lift-off model presented by Sturgis and Mudawar [11] is modified to incorporate the effects of body force as well as a new statistical interfacial curvature parameter. The reader should refer to Ref. [11] for details of the interfacial lift-off model not included in this paper.

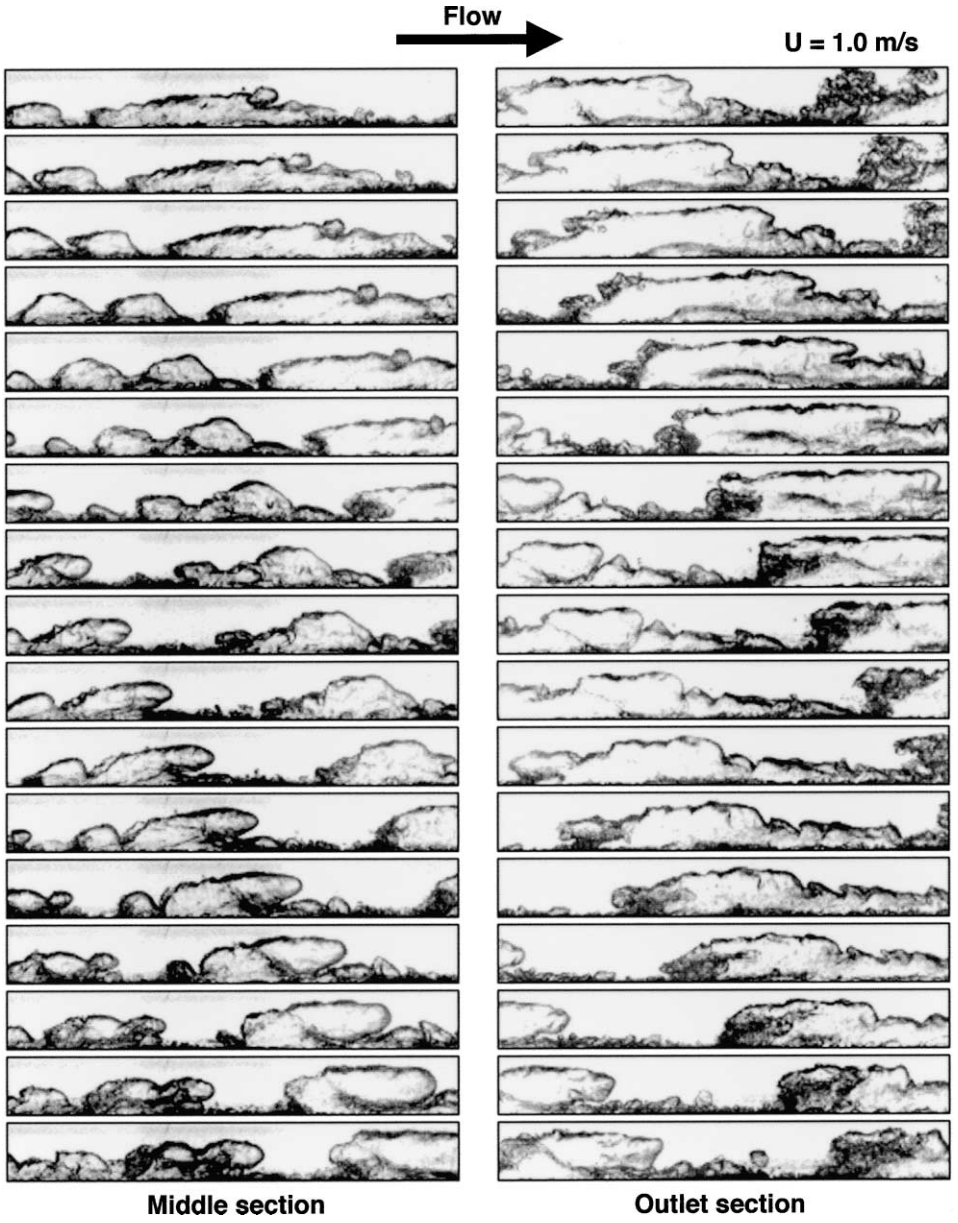

Fig. 5. Sequential images of wavy vapor layer at $\theta = 135°$, $\Delta T_{sub,o} = 3$ °C and $U = 1$ m/s.

4.2. Interfacial instability of vapor layer

Describing interfacial instability of the vapor layer requires knowledge of the mean liquid velocity, U_f, mean vapor velocity, U_g, and mean vapor layer thickness, δ. A two-phase separated flow model is employed to determine these parameters.

In this model, the heat supplied between the leading edge of the heated wall and a location z is assumed to bring a mass of liquid to saturation temperature and then convert the same mass to saturated vapor. Energy conservation leads to the following expression for vapor velocity, U_g, in terms of the average wall heat flux,

$$U_g = \frac{q''z}{\rho_g \delta \left(c_{p,f}\Delta T_{sub,i} + h_{fg}\right)}. \tag{5}$$

The liquid velocity, U_f, can be determined from mass conservation by subtracting the rate of mass conversion to vapor from the total mass flow rate at the channel inlet.

$$U_f = \frac{UH}{H-\delta} - \frac{q''z}{\rho_f (H-\delta)\left(c_{p,f}\Delta T_{sub,i} + h_{fg}\right)}. \tag{6}$$

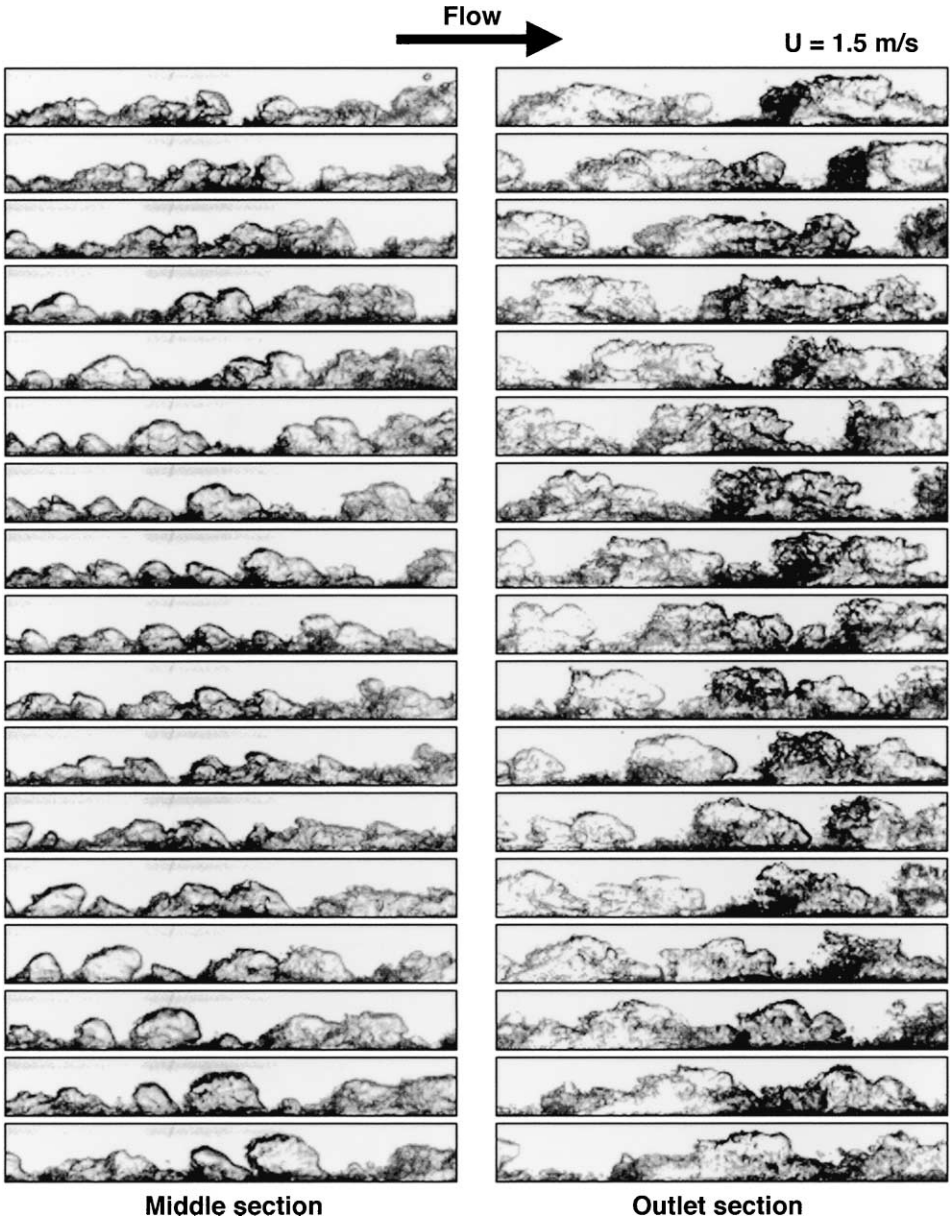

Fig. 6. Sequential images of wavy vapor layer at $\theta = 135°$, $\Delta T_{sub,o} = 3$ °C and $U = 1.5$ m/s.

Conservation of momentum for a section Δz of the separated two-phase flow may be applied to control volumes encompassing the liquid (volume $A_f \Delta z$) and vapor (volume $A_g \Delta z$) separately, resulting, respectively, in the following equations:

$$\frac{d}{dz}\left(\rho_f U_f^2 A_f\right) + W'_{fg} u_i = -A_f \frac{dP}{dz} - \tau_{w,f} p_{w,f} + \tau_i p_i - \rho_f A_f g \sin\theta \quad (7)$$

and

$$\frac{d}{dz}\left(\rho_g U_g^2 A_g\right) - W'_{fg} u_i = -A_g \frac{dP}{dz} - \tau_{w,g} p_{w,g} - \tau_i p_i - \rho_g A_g g \sin\theta, \quad (8)$$

where W'_{fg} is the rate of evaporation per unit distance, u_i is the streamwise velocity of the vapor formed at the interface, $\tau_{w,f}$, $\tau_{w,g}$, and τ_i are respectively, the wall shear stress in the liquid, wall shear stress in the vapor, and interfacial shear stress, and $p_{w,f}$, $p_{w,g}$ and p_i are the perimeter of liquid contact with the channel wall, perimeter of vapor contact with the channel wall, and

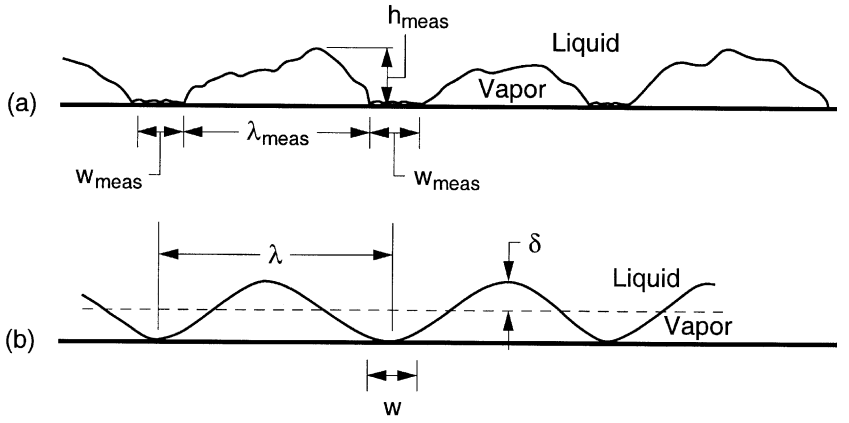

Fig. 7. Definitions of vapor layer dimensions for (a) flow visualization study and (b) idealized wavy vapor layer in CHF model.

Table 1
Statistically determined interfacial characteristics of wavy vapor layer

Orientation θ	Middle section				Outlet section			
	δ (mm)	λ (mm)	w (mm)	$b = w/\lambda$	δ (mm)	λ (mm)	w (mm)	$b = w/\lambda$
$U = 1$ m/s								
90°	1.95	15.13	3.48	0.23	2.26	18.77	4.10	0.22
135°	1.78	19.09	4.20	0.22	1.95	14.39	3.14	0.22
180°	1.54	10.33	2.39	0.23	1.82	17.25	3.79	0.22
225°	1.31	8.81	2.18	0.24	1.74	21.08	4.48	0.21
270°	1.27	6.03	1.34	0.22	1.93	15.26	3.21	0.21
$U = 1.5$ m/s								
0°	1.57	6.11	1.36	0.22	2.13	11.73	2.86	0.25
90°	1.72	11.28	2.45	0.21	2.01	16.03	3.32	0.21
135°	1.70	8.79	1.80	0.23	1.81	13.61	3.04	0.22
180°	1.53	10.41	2.33	0.22	1.79	20.07	4.50	0.22
225°	1.44	12.91	3.00	0.23	1.89	18.92	3.88	0.21
270°	1.39	6.32	1.39	0.22	1.79	12.76	2.96	0.23

perimeter of liquid–vapor contact (equal to channel width W), respectively.

The present model assumes that vapor generated at the wall has no initial streamwise velocity ($u_i \approx 0$) [9] and, as such, does not contribute streamwise momentum to the control volume. Introducing flow quality, x, and void fraction, α, into Eqs. (7) and (8) yields, respectively,

$$G^2 \frac{\mathrm{d}}{\mathrm{d}z}\left[\frac{(1-x)^2}{\rho_f(1-\alpha)}\right] = -(1-\alpha)\frac{\mathrm{d}P}{\mathrm{d}z} - \frac{\tau_{w,f} p_{w,f}}{A} + \frac{\tau_i p_i}{A} - \rho_f(1-\alpha) g \sin\theta \quad (9)$$

and

$$G^2 \frac{\mathrm{d}}{\mathrm{d}z}\left(\frac{x^2}{\rho_g \alpha}\right) = -\alpha\frac{\mathrm{d}P}{\mathrm{d}z} - \frac{\tau_{w,g} p_{w,g}}{A} - \frac{\tau_i p_i}{A} - \rho_g \alpha g \sin\theta, \quad (10)$$

where

$$x = \frac{\rho_g U_g \alpha}{G} \quad (11)$$

and $\alpha = \delta/H$.

Eq. (10) can be rearranged to yield a pressure gradient for the vapor layer expressed as the sum of accelerational, frictional, and gravitational components.

$$-\frac{\mathrm{d}P_g}{\mathrm{d}z} = \left(-\frac{\mathrm{d}P_g}{\mathrm{d}z}\right)_A + \left(-\frac{\mathrm{d}P_g}{\mathrm{d}z}\right)_F + \left(-\frac{\mathrm{d}P_g}{\mathrm{d}z}\right)_G = \frac{G^2}{\alpha}\frac{\mathrm{d}}{\mathrm{d}z}\left(\frac{x^2}{\alpha\rho_g}\right) + \frac{\tau_{w,g}}{\alpha}\left[\frac{1}{H} + \frac{2}{W}\alpha\right] + \frac{\tau_i}{\alpha}\frac{1}{H} + \rho_g g \sin\theta. \quad (12)$$

Adding Eqs. (9) and (10) yields a pressure gradient for the combined flow (liquid and vapor) which can also

be expressed as the sum of accelerational, frictional, and gravitational components.

$$-\frac{dP}{dz} = \left(-\frac{dP}{dz}\right)_A + \left(-\frac{dP}{dz}\right)_F + \left(-\frac{dP}{dz}\right)_G = G^2 \frac{d}{dz}\left(\frac{x^2}{\alpha\rho_g} + \frac{(1-x)^2}{(1-\alpha)\rho_f}\right) + \tau_{w,g}\left[\frac{1}{H} + \frac{2}{W}\alpha\right] + \tau_{w,f}\left[\frac{1}{H} + \frac{2}{W}(1-\alpha)\right] + \left[\alpha\rho_g + (1-\alpha)\rho_f\right] g\sin\theta. \quad (13)$$

The wall shear stress terms in Eqs. (12) and (13) can be expressed in terms of a friction factor,

$$\tau_{w,k} = \frac{1}{2}\rho_k U_k^2 \left(\frac{f_k}{4}\right), \quad (14)$$

where k indicates the phase, and the friction factor is given by [11]

$$f_k = 0.184\left(\frac{\rho_k U_k D_{h,k}}{\mu_k}\right)^{-1/5}, \quad (15)$$

and $D_{h,k}$ is the hydraulic diameter for each phase. The interfacial shear stress term in Eq. (12) is defined as

$$\tau_i = \frac{C_{f,i}}{2}\rho_g (U_g - U_f)^2. \quad (16)$$

Galloway and Mudawar [9] examined several models for the interfacial friction coefficient, $C_{f,i}$, and recommended a constant value of 0.5 for a wavy vapor–liquid interface.

Equating the pressure gradients in Eqs. (12) and (13) yields an equation which can be solved along with Eqs. (5) and (6) to determine the variations of U_f, U_g and δ with z.

The observed liquid–vapor interface can be idealized as a sinusoidal wave of the form

$$\eta(z,t) = \eta_0 e^{ik(z-ct)}, \quad (17)$$

where η_0 represents the wave amplitude ($\eta_0 = \delta$), k the wave number ($k = 2\pi/\lambda$), and c the wave speed. Using classical instability theories [9,11,17], the pressure difference resulting from a small disturbance perpendicular to the interface can be expressed as

$$P_f - P_g = -\left[\rho_f''(c - U_f)^2 + \rho_g''(c - U_g)^2 + (\rho_f - \rho_g)\frac{g_n}{k}\right] k\eta_0 e^{ik(z-ct)}, \quad (18)$$

where $\rho_f'' = \rho_f \coth(kH_f)$ and $\rho_g'' = \rho_g \coth(kH_g)$ ("modified density" terms), and g_n is the component of gravity perpendicular to, and pointing towards the heated wall. The pressure difference can be related to the surface tension force by

$$P_f - P_g \approx \sigma\frac{\partial^2\eta}{\partial z^2} = -\sigma\eta_0 k^2 e^{ik(z-ct)}. \quad (19)$$

Equating pressure difference in Eqs. (18) and (19) yields an expression for the wave speed, c.

$$c = \frac{\rho_f'' U_f + \rho_g'' U_g}{\rho_f'' + \rho_g''} \pm \sqrt{\frac{\sigma k}{\rho_f'' + \rho_g''} - \frac{\rho_f''\rho_g''(U_g - U_f)^2}{(\rho_f'' + \rho_g'')^2} - \frac{(\rho_f - \rho_g)}{(\rho_f'' + \rho_g'')}\frac{g\cos\theta}{k}}. \quad (20)$$

A negative argument in the radical of Eq. (20) results in a wave speed containing both real and imaginary components. The imaginary component

$$c_i = \sqrt{\frac{\rho_f''\rho_g''(U_g - U_f)^2}{(\rho_f'' + \rho_g'')^2} + \frac{(\rho_f - \rho_g)}{(\rho_f'' + \rho_g'')}\frac{g\cos\theta}{k} - \frac{\sigma k}{\rho_f'' + \rho_g''}} \quad (21)$$

represents the combined effect of the different forces and determines the stability of the interface. The first term under the radical in Eq. (21) is a measure of the destabilizing effect of velocity difference between the liquid and vapor phases. The second term is the body force effect, which may be stabilizing or destabilizing depending on orientation of the wall relative to gravity. The third term accounts for surface tension which is always stabilizing to the interface.

The critical wavelength, defined as the wavelength of a neutrally stable wave, can be determined by setting the radical in Eq. (21) equal to zero.

$$k_c = \frac{2\pi}{\lambda_c} = \frac{\rho_f''\rho_g''(U_g - U_f)^2}{2\sigma(\rho_f'' + \rho_g'')} + \sqrt{\left[\frac{\rho_f''\rho_g''(U_g - U_f)^2}{2\sigma(\rho_f'' + \rho_g'')}\right]^2 + \frac{(\rho_f - \rho_g)g\cos\theta}{\sigma}}. \quad (22)$$

Fig. 8 shows the dependence of critical wavelength, λ_c, on the velocity difference and flow orientation. Different values of velocity difference are assumed to explore the λ_c trends. For low velocities, there exists an orientation range over which the interface is always stable. This should produce a fairly smooth vapor layer along the heated wall and preclude any liquid contact, greatly reducing CHF for these orientations and low velocity differences. This was indeed observed by the authors in [16]. Interestingly, even with an unstable wave that provides the necessary liquid contact in wetting fronts, Fig. 8 shows low velocity differences both exhibit high sensitivity to orientation and produce unusually large wavelengths. At 0.1 m/s, the critical wavelength engulfs a large fraction of the heated length, meaning very low velocity differences can cause dryout of a considerable fraction of the heated area and induce CHF prema-

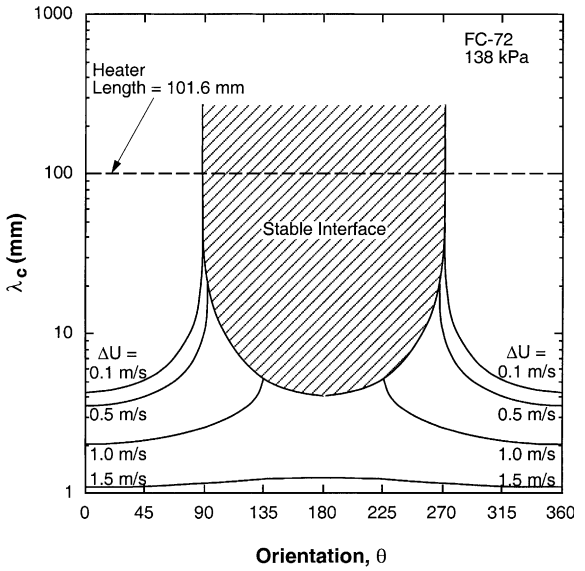

Fig. 8. Variation of predicted critical wavelength with flow orientation for different velocity differences.

turely. These large wavelengths are also consistent with the observations of the authors in [16]. Finally, Fig. 8 shows increasing velocity reduces the sensitivity of λ_c to body force by imparting dominance to the inertia term in Eq. (21) compared to the body force term. For high-velocities, Eq. (22) shows λ_c will approach the limit

$$\lambda_c = \frac{2\pi\sigma\left(\rho_f'' + \rho_g''\right)}{\rho_f''\rho_g''\left(U_g - U_f\right)^2} \tag{23}$$

irrespective of body force.

4.3. Interfacial lift-off

As indicated earlier, interfacial lift-off is postulated to occur when the momentum flux of vapor emanating from the wetting front just exceeds the pressure force acting upon the interface. The pressure force is the result of the difference between liquid and vapor pressures across the curved interface. Fig. 9 illustrates these two opposing effects.

The pressure force over the entire wetting front is obtained by integrating Eq. (18) over the length $b\lambda$ centered at the wetting front.

$$\overline{P_f - P_g} = \frac{4\pi\sigma\delta}{b\lambda^2}\sin(b\pi). \tag{24}$$

The heat supplied in the wetting front is consumed by vaporizing liquid into vapor according the relation

$$q_w'' A_w = \left(c_{p,f}\Delta T_{sub,i} + h_{fg}\right)\rho_g U_{g,n} A_w, \tag{25}$$

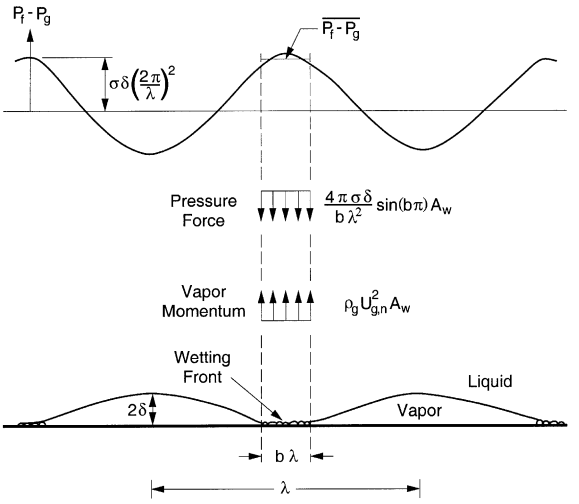

Fig. 9. Balance of vapor momentum and interfacial pressure difference used to determine lift-off heat flux.

where $U_{g,n}$ is the vapor velocity in the wetting front normal to the wall. Eq. (25) yields

$$U_{g,n} = \frac{q_w''}{\rho_g\left(c_{p,f}\Delta T_{sub,i} + h_{fg}\right)}. \tag{26}$$

The local lift-off heat flux can be determined by equating the vapor momentum, $\rho_g U_{g,n}^2$, to the pressure force.

$$\begin{aligned} q_w'' &= \rho_g\left(c_{p,f}\Delta T_{sub,i} + h_{fg}\right)\sqrt{\frac{\overline{P_f - P_g}}{\rho_g}} \\ &= \rho_g\left(c_{p,f}\Delta T_{sub,i} + h_{fg}\right)\left[\frac{4\pi\sigma}{\rho_g}\frac{\sin(b\pi)}{b}\right]^{1/2}\frac{\delta^{1/2}}{\lambda}. \end{aligned} \tag{27}$$

Eq. (27) shows the lift-off heat flux, q_w'', is proportional to $\delta^{1/2}\lambda$, which can be viewed as a measure of interfacial curvature.

Flow visualization revealed the existence of a continuous wetting region near the leading edge, where the liquid maintains contact with the heated wall. The length of the upstream continuous wetting region, z^*, may be defined as

$$z^* = z_0 + \lambda_c(z^*), \tag{28}$$

where z_0 is the location measured from the leading edge where the vapor velocity just surpasses the liquid velocity [11]. Hydrodynamic instability generates the wavy interface at z^*, downstream from which the wavy vapor layer begins to propagate along the heated wall.

The flow visualization measurements revealed the interfacial wavelengths increase is the flow direction, as shown in Fig. 10(a) and (b) for $U = 1$ and 1.5 m/s, respectively. Wavelengths in the middle and outlet sections

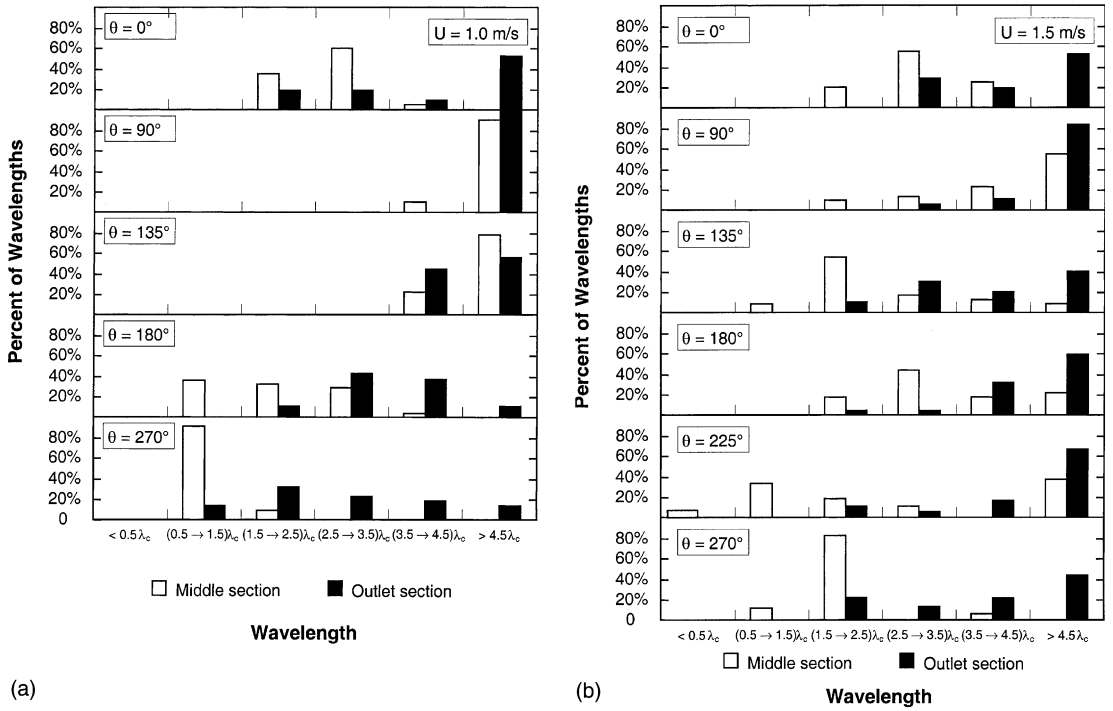

Fig. 10. Distribution of wavelengths measured in middle and outlet sections of heated wall relative to critical wavelength predicted at z^* for (a) $U = 1$ m/s and (b) $U = 1.5$ m/s.

of the heater grow to over four times their critical value at z^*.

The wave curvature parameter $\delta^{1/2}/\lambda$ was also calculated from the flow visualization measurements in the middle and outlet sections of the heated length for $U = 1$ and 1.5 m/s; the results are shown in Fig. 11(a) and (b), respectively. Several important conclusions can be drawn from these plots. First, the waves in the outlet section are slightly flatter (i.e., characterized by weaker curvature) than those in the middle section since the outlet section's $\delta^{1/2}/\lambda$ values are somewhat smaller. The outlet waves are therefore easier to lift off from the heated wall. Thus, CHF is more likely to occur in the outlet section. This was confirmed in the present study by consistent CHF detection by the outlet thermocouple array first for CHF conditions belonging to the wavy vapor layer regime. Overall, however, Fig. 11a and b show the majority of $\delta^{1/2}/\lambda$ values for both the middle and outlet sections range from $0.5(\delta^{1/2}/\lambda_c)$ to $1.5(\delta^{1/2}/\lambda_c)$, where both δ and λ_c are calculated at z^*. Therefore, these waves, which are generated upstream at z^*, have a tendency to preserve their curvature value as they propagate along the heated wall.

Measurements also reveal that the wetting front length increases in the flow direction while remaining a constant fraction of the local wavelength,

$$w_j = b\lambda_j. \tag{29}$$

For the present model, $b = 0.20$ is used based on both the present flow visualization measurements and for consistency with Sturgis and Mudawar statistical results [11].

Prior to CHF, liquid makes contact with the heated wall only in the wetting fronts. With the definition of critical heat flux, q''_m, as the average heat flux over the entire heated wall, an energy balance for the outlet section gives

$$q''_m = bq''_w. \tag{30}$$

Combining Eqs. (27) and (30) gives

$$q''_m = \rho_g\left(c_{p,f}\Delta T_{sub,i} + h_{fg}\right)\left[\frac{4\pi\sigma b\sin(b\pi)}{\rho_g}\right]^{1/2}\left.\frac{\delta^{1/2}}{\lambda_c}\right|_{z^*}, \tag{31}$$

where both δ and λ_c are calculated at z^* since $\delta^{1/2}/\lambda$ in the outer section and at z^* are equal.

4.4. Model predictions

An iterative numerical technique is used to calculate CHF. First, an estimated value for CHF is used in the

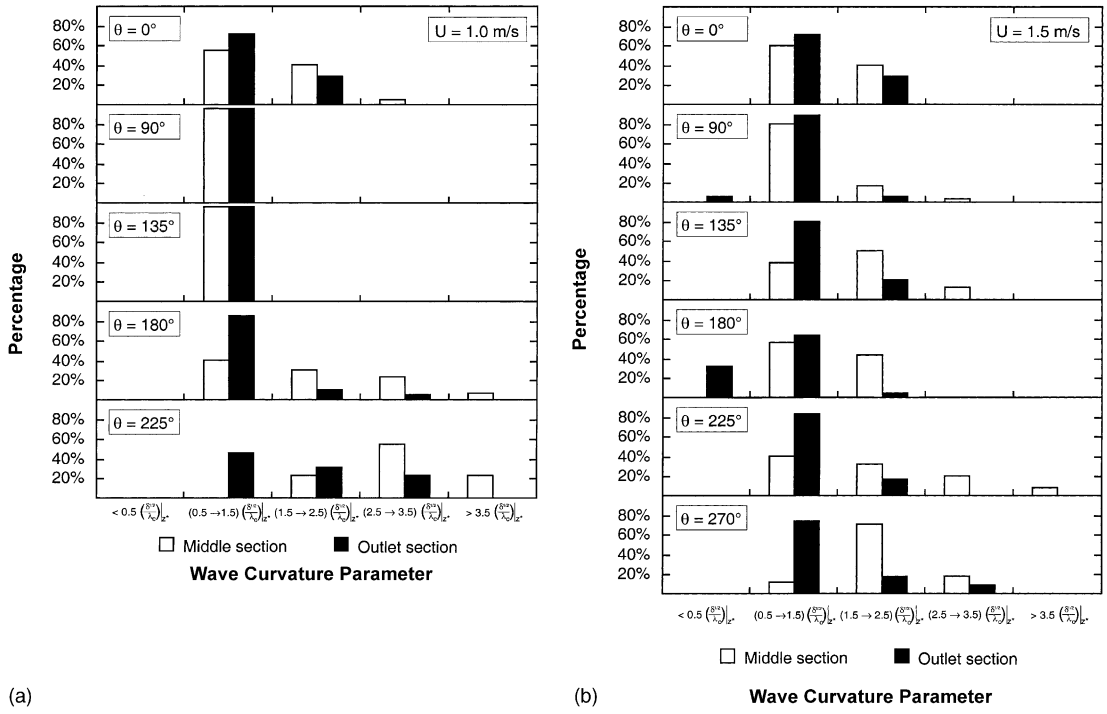

Fig. 11. Distribution of wave curvature parameter in middle and outlet sections of heated wall compared with its value at z^* for (a) $U = 1$ m/s and (b) $U = 1.5$ m/s.

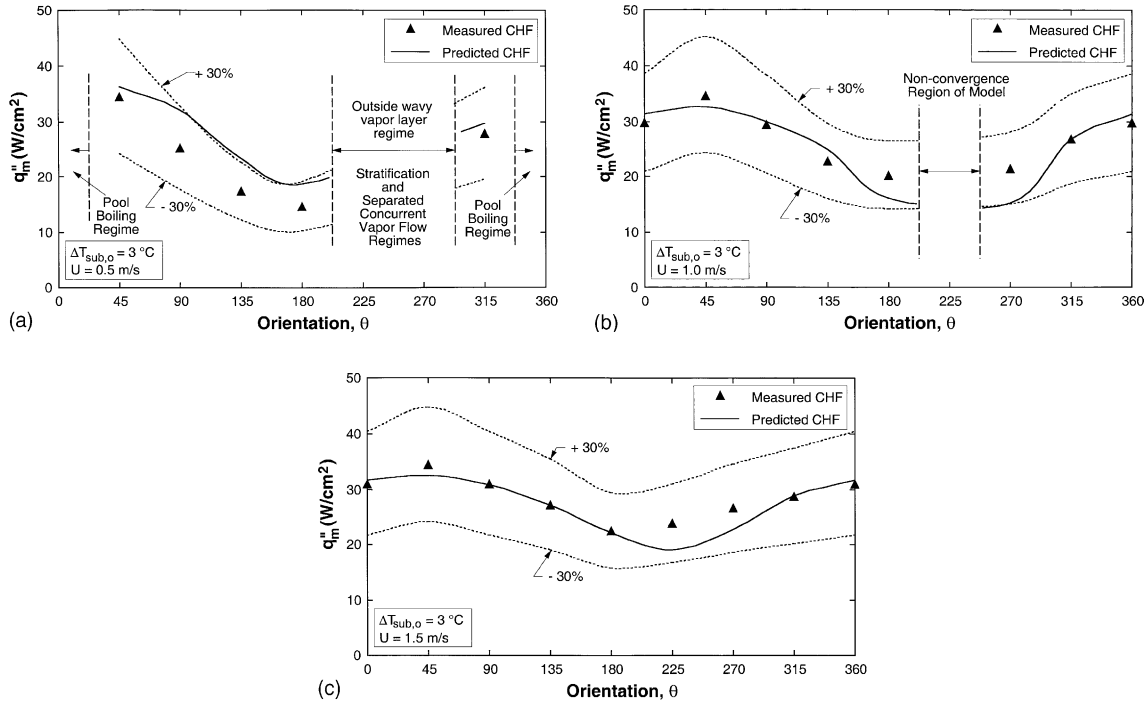

Fig. 12. Comparison of measured and predicted CHF for (a) $U = 0.5$ m/s, (b) $U = 1$ m/s and (c) $U = 1.5$ m/s.

separated flow model to determine the variations of phase velocities, U_f and U_g, and vapor layer thickness, δ, with z. The output of the separated flow model is then utilized in the instability analysis to determine z^* and the critical wavelength, λ_c, at z^*. Eq. (31) was then used to calculate a new CHF value. This value is input into the separated flow model in the next iteration. The solution is deemed convergent once the CHF values of consecutive iterations are matched.

The model was applied to near-saturated conditions corresponding to the entire wavy vapor layer regime. The predicted and measured CHF values are compared in Fig. 12(a)–(c) for three velocities. The predictions capture the overall shape of CHF variation with orientation angle quite well, with predictions falling mostly within a ±30% error band. The mean absolute error of the model predictions from the data is 20%, 9.8% and 5.4% for $U = 0.5$, 1 and 1.5 m/s, respectively.

Fig. 12(a) shows a specific range of downflow orientations for which the CHF model will not converge for $U = 0.5$ m/s. Fig. 8 shows this orientation range may yield a stable interface, and, according to Fig. 2, fall into stratification or separated concurrent vapor flow regimes. Fig. 12(b) shows similar limitations of the present model near $\theta = 225°$ for $U = 1$ m/s.

5. Conclusions

This study involved both experimental and theoretical investigation of the effects of orientation on flow boiling CHF. High-speed video and microphotographic techniques were used to measure interfacial features just prior to CHF. The measured features were statistically analyzed and incorporated into the model. Key findings from the study are as follows:

(1) Six different CHF regimes were observed. A dominant wavy vapor layer regime was observed for all relatively high-velocities and most orientations, while all the other regimes were encountered at low velocities, in downflow and/or downward-facing heated wall orientations. The present CHF model is intended only for the dominant wavy vapor layer regime.
(2) Video analysis of the wavy vapor layer supports Galloway and Mudawar's [8,9] depiction of a fairly continuous wavy vapor layer travelling along the wall while permitting liquid contact only in wetting fronts, located in the troughs of the interfacial waves.
(3) An instability model of the wavy vapor layer interface shows low phase velocity differences produce a stable interface for certain orientations, precluding liquid contact with the heated wall and resulting in very low CHF values. Even with an unstable wave that provides the necessary liquid contact, low phase velocity differences produce unusually large wavelengths capable of engulfing a large fraction of the heated length. Increasing phase velocity difference reduces the sensitivity of critical wavelength to body force by imparting dominance to liquid inertia over body force.
(4) Interfacial measurements reveal both the wavelength and wetting front length increase in the flow direction but their ratio remains constant.
(5) Lift-off of wetting fronts is closely related to a wave curvature parameter $\delta^{1/2}/\lambda$. Measurements reveal waves in the outlet section of the heated wall are slightly flatter that those in the middle section, and therefore are easier to lift off. This was confirmed by consistent CHF detection in the outlet section. Overall, however, the waves, which are generated at an upstream location, have a tendency to preserve their curvature value as they propagate along the heated wall.
(6) The interfacial lift-off model is very effective at capturing the overall dependence of CHF on orientation. The mean absolute error of the model predictions from the data is 20%, 9.8%‘ and 5.4% for $U = 0.5$, 1 and 1.5 m/s, respectively. For the lower velocities, the model is not valid for certain downflow orientations which are associated with a stable interface.

Acknowledgements

The authors are grateful for the support of the National Aeronautics and Space Administration under grant no. NAG3-2336.

References

[1] S.S. Kutateladze, A.I. Leont'ev, Some applications of the asymptotic theory of the turbulent boundary layer, in: Proceeding of the 3rd International Heat Transfer Conference, Chicago, Illinois, Vol. 3, 1966, pp. 1–6.
[2] L.S. Tong, Boundary-layer analysis of the flow boiling crisis, Int. J. Heat Mass Transfer 11 (1968) 1208–1211.
[3] W. Hebel, W. Detavernier, M. Decreton, A contribution to the hydrodynamics of boiling crisis in a forced flow of water, Nucl. Eng. Des. 64 (1981) 443–445.
[4] J. Weisman, B.S. Pei, Prediction of critical heat flux in flow boiling at low qualities, Int. J. Heat Mass Transfer 26 (1983) 1463–1477.
[5] C.H. Lee, I. Mudawar, A mechanistic critical heat flux model for subcooled flow boiling based on local bulk flow conditions, Int. J. Multiphase Flow 14 (1988) 711–728.
[6] R. Hino, T. Ueda, Studies on heat transfer and flow characteristics in subcooled flow boiling—part 1. Boiling

characteristics, Int. J. Multiphase Flow 11 (1985a) 269–281.

[7] R. Hino, T. Ueda, Studies on heat transfer and flow characteristics in subcooled flow boiling—part 2. Flow characteristics, Int. J. Multiphase Flow 11 (1985b) 283–297.

[8] J.E. Galloway, I. Mudawar, CHF mechanism in flow boiling from a short heated wall—part 1. Examination of near-wall conditions with the aid of photomicrography and high-speed video imaging, Int. J. Heat Mass Transfer 36 (1993) 2511–2526.

[9] J.E. Galloway, I. Mudawar, CHF mechanism in flow boiling from a short heated wall—part 2. Theoretical CHF model, Int. J. Heat Mass Transfer 36 (1993) 2527–2540.

[10] J.C. Sturgis, I. Mudawar, Critical heat flux in a long, rectangular channel subjected to one-sided heating—I. Flow visualization, Int. J. Heat Mass Transfer 42 (1999) 1835–1847.

[11] J.C. Sturgis, I. Mudawar, Critical heat flux in a long, rectangular channel subjected to one-sided heating—II. Analysis of critical heat flux data, Int. J. Heat Mass Transfer 42 (1999) 1849–1862.

[12] A.H. Howard, I. Mudawar, Orientation effects on pool boiling critical heat flux (CHF) and modeling of CHF for near-vertical surfaces, Int. J. Heat Mass Transfer 42 (1999) 1665–1688.

[13] N. Zuber, M. Tribus, J.W. Westwater, The hydrodynamic crisis in pool boiling of saturated and subcooled liquids, International Developments in Heat Transfer: Proceedings of 1961–62 International Heat Transfer Conference, Boulder, CO, 1961, pp. 230–236.

[14] R.J. Simoneau, F.F. Simon, A visual study of velocity and buoyancy effects on boiling Nitrogen, NASA Tech Note TN D-3354, 1966.

[15] K. Mishima, H. Nishihara, The effect of flow direction and magnitude on CHF for low pressure water in thin rectangular channels, Nucl. Eng. Des. 86 (1985) 165–181.

[16] H. Zhang, I. Mudawar, M.M. Hasan, Experimental assessment of flow boiling CHF in reduced gravity using different flow channel orientations in 1-g ground-based experiments, Int. J. Heat Mass Transfer, in review.

[17] L.M. Milne-Thomson, Theoretical Hydrodynamics, fourth ed., MacMillan, New York, 1960.